Int J Earth Sci (Geol Rundsch) (2016) 105:2133–2148
DOI 10.1007/s00531-016-1324-1

ORIGINAL PAPER

Crustal structure of the northern Menderes Massif, western Turkey, imaged by joint gravity and magnetic inversion

Klaus Gessner[1] · Luis A. Gallardo[2] · Francis Wedin[3] · Kerim Sener[3]

Received: 31 August 2015 / Accepted: 31 March 2016 / Published online: 23 May 2016

Abstract In western Anatolia, the Anatolide domain of the Tethyan orogen is exposed in one of the Earth's largest metamorphic core complexes, the Menderes Massif. The Menderes Massif experienced a two-stage exhumation: tectonic denudation in the footwall of a north-directed Miocene extensional detachment, followed by fragmentation by E–W and NW–SE-trending graben systems. Along the northern boundary of the core complex, the tectonic units of the Vardar–Izmir–Ankara suture zone overly the stage one footwall of the core complex, the northern Menderes Massif. In this study, we explore the structure of the upper crust in the northern Menderes Massif with cross-gradient joint inversion of gravity and aeromagnetic data along a series of 10-km-deep profiles. Our inversions, which are based on gravity and aeromagnetic measurements and require no geological and petrophysical constraints, reveal the salient features of the Earth's upper crust. We image the northern Menderes Massif as a relatively homogenous domain of low magnetization and medium to high density, with local anomalies related to the effect of interspersed igneous bodies and shallow basins. In contrast, both the northern and western boundaries of the northern Menderes Massif stand out as domains where dense mafic, metasedimentary and ultramafic domains with a weak magnetic signature alternate with low-density igneous complexes with high magnetization. With our technique, we are able to delineate Miocene basins and igneous complexes, and map the boundary between intermediate to mafic-dominated subduction–accretion units of the suture zone and the underlying felsic crust of the Menderes Massif. We demonstrate that joint gravity and magnetic inversion are not only capable of imaging local and regional changes in crustal composition, but can also be used to map discontinuities of geodynamic significance such as the Vardar–Izmir–Ankara suture and the West Anatolia Transfer Zone.

Keywords Geophysical inversion · Gravity anomaly · Magnetic anomaly · Menderes Massif · Turkey · Metamorphic core complex · Suture zone · Ophiolite

Introduction

Cross-gradient joint geophysical inversion is emerging as a preferred strategy for integrated studies of the subsurface (e.g. Gallardo and Meju 2011; Haber and Gazit 2013). It is based on the assumption of a common structural framework in fully heterogeneous models and has been used successfully for geophysical exploration in a number of geological settings (Gallardo and Meju 2011; Gallardo and Thebaud 2012; Gallardo et al. 2012). In this study, we explore if it is possible to structurally harmonize gravity and magnetic evidence to characterize the upper crust of the northern Menderes Massif. The

Electronic supplementary material The online version of this article (doi:10.1007/s00531-016-1324-1) contains supplementary material, which is available to authorized users.

✉ Klaus Gessner
klaus.gessner@uwa.edu.au

[1] Centre for Exploration Targeting, School of Earth Sciences, The University of Western Australia, 35 Stirling Highway, Crawley 6009, Australia

[2] Earth Science Division, CICESE, Carretera Ensenada-Tijuana No. 3918, CP 22860 Ensenada, Mexico

[3] Ariana Resources Plc, Bridge House, London Bridge, London SE1 9QR, UK

Menderes Massif, one of Earth's largest metamorphic core complexes, exposes the lower crustal levels of the Anatolide segment of the Tethyan orogen. The structural complexity, which is only partially understood, is a result of a series of tectonic events that include Neoproterozoic to Cambrian and Eocene to recent orogenic processes (Gessner et al. 2013, and references therein). Since the Miocene, the Menderes Massif experienced tectonic denudation and surface uplift in the footwall of a north-directed Miocene extensional detachment system, followed by fragmentation by E–W and NW–SE-trending graben systems (e.g. Hancock and Barka 1987; Gessner et al. 2001a, 2013). In the northern part of the core complex, the tectonic units of a Neotethys suture zone overly the stage one footwall of the core complex, the northern Menderes Massif. The complexity of deformation and its protracted Cenozoic magmatic history provide a formidable challenge to unravel its geological history. Understanding the structure of the northern Menderes Massif, however, is fundamental to deciphering the regional tectonic history and assessing its economic potential for mineral and energy resources (Yilmaz 1981; Oyman et al. 2003; Yigit 2006; Yilmaz et al. 2007; Faulds et al. 2009; Sener et al. 2009; Yigit 2009). Here, we present a series of profiles based on joint gravity and magnetic inversion that highlight the structure of the upper crust across the northern Menderes Massif, image basins and igneous complexes, and help constrain the geometry of the Neotethyan suture zone.

Tectonic setting

In western Anatolia, Cretaceous to Palaeogene subduction–accretion complexes constitute the hanging wall of the Vardar–Izmir–Ankara suture, including the Tavşanlı zone and the Bornova Flysch zone (Fig. 1) (Okay and Tüysüz 1999; Okay 2011; Gessner et al. 2013). The Afyon–Ören zone and the Lycian nappes (Okay and Tüysüz 1999; Pourteau et al. 2010) occur structurally below the ophiolitic parts of the Vardar–Izmir–Ankara zone units, parts of which may constitute remains of a separate, continuous Anatolian ophiolite nappe (Okay 2010).

We follow the tectonic division of the Menderes Massif as an Alpine nappe stack that has recorded a polyorogenic history, which extends back into the Neoproterozoic to Cambrian (Kröner and Sengör 1990; Hetzel and Reischmann 1996; Ring et al. 1999; Candan et al. 2001; Gessner et al. 2001b; Regnier et al. 2003; Gessner et al. 2004; Ring et al. 2004; Catlos and Çemen 2005; Ring and Collins 2005; Cemen et al. 2006; Oberhänsli et al. 2010; Candan et al. 2011; Zlatkin et al. 2013), but lacks Eocene high-pressure metamorphic overprint in structural deeper units (Gessner et al. 2001c).

North–south extension in the central Aegean Sea region and in the Anatolide Belt of western Anatolia started around the Oligocene–Miocene boundary (Schermer et al. 1990; Seyitoglu and Scott 1996), but the overall magnitude of extension differs significantly in both regions. The Aegean is largely submerged with the Cycladic archipelago representing a horst structure between the more highly extended northern Aegean Sea and the Cretan Sea. Western Anatolia is characterized by thicker crust than the Aegean (Makris and Stobbe 1984; Tirel et al. 2004; Özeren and Holt 2010; Mutlu and Karabulut 2011). A boundary between the Aegean and Anatolian domains has been proposed based on the differences in extension geometry and metamorphic history (Ring et al. 1999), as well as on the occurrence of NNE-trending fault systems and basins in western Anatolia (Sözbilir et al. 2003; Özkaymak and Sozbilir 2008; Uzel and Sozbilir 2008; Erkül 2010), where it has been named the İzmir–Balıkesir Transfer Zone (Erkül 2010). Here, we follow the interpretation of Gessner et al. (2013) that the boundary between the Aegean and Anatolian domains is a lithosphere-scale structure, the West Anatolia Transfer Zone (WATZ).

Crustal extension in western Anatolia is expressed by normal fault systems of Miocene to recent age (Hancock and Barka 1987; Cohen et al. 1995; Hetzel et al. 1995a, b; Gessner et al. 2001b; Isik and Tekeli 2001; Ring and Collins 2005; Emre and Sözbilir 2007; Glodny and Hetzel 2007; Erkül 2010). The Menderes Massif has experienced a two-stage cooling history. The Central Menderes Metamorphic Core Complex (CMCC) represents the 'inner' axial core, where the lowest structural levels of the Anatolide Belt were exposed in the footwall of opposite-facing Miocene to Pliocene detachment faults (Figs. 1, 2). The two 'outer' submassifs, the Gördes submassif to the north (in this study referred to as the northern Menderes Massif) and the Çine submassif to the south, represent higher levels of the nappe stack that cooled during the latest Oligocene and early Miocene (Gessner et al. 2001b; Ring et al. 2004; Gessner et al. 2013) (Fig. 2). In the northern Menderes Massif, cooling occurred as a consequence of rapid tectonic denudation during N to NNE-directed movement on the Simav and Alacamdağ detachment systems (Isik and Tekeli 2001; Ring and Collins 2005; Erkül 2010; Catlos et al. 2012). In this area, apatite fission track ages show a northward younging trend in the direction of hanging wall movement of the detachments (Thomson and Ring 2006; Gessner et al. 2013). Ophiolitic klippen that directly overly Çine nappe orthogneiss across the northern Menderes Massif and a large age gap in apatite fission track data across the contact between the Menderes Massif and the overlying Tavşanlı zone (Gessner et al. 2013) suggests that large parts of the Alpine nappe stack have been cut out by the early Miocene Simav—Alaçamdağ detachment system (Isik and

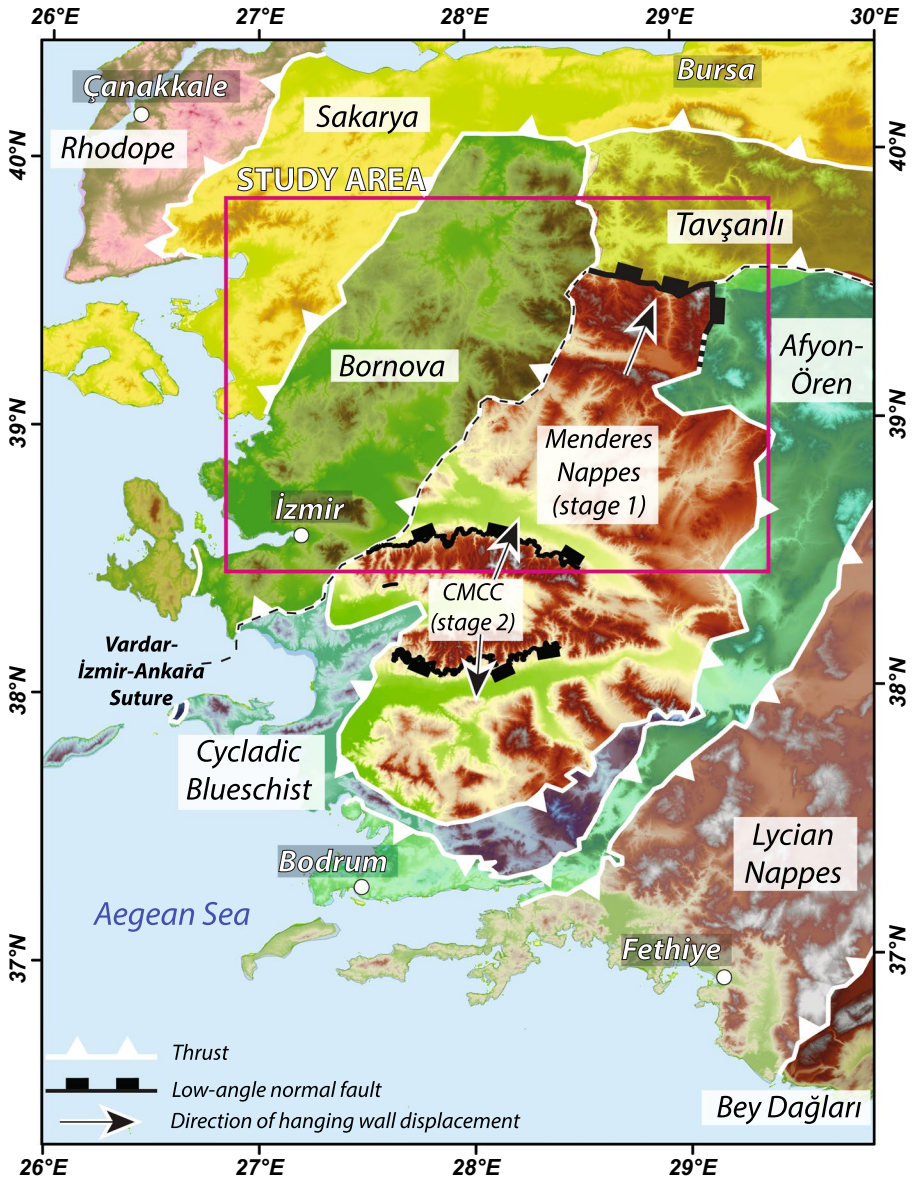

Fig. 1 Tectonic units of western Turkey after Gessner et al. (2013). The Menderes Massif is the structurally lowest part of the Tethyan orogen in western Anatolia. Early Miocene extensional detachments at the northern boundary define stage 1 of northeast stretching and tectonic denudation. During stage 2, the Central Menderes Metamorphic Core Complex (CMCC) formed within the stage one lower plate

Tekeli 2001; Ring and Collins 2005; Thomson and Ring 2006; Erkül 2010).

The northern Menderes Massif is characterized by alternating northeast-trending Miocene sedimentary basins and basement highs that typically expose Çine nappe orthogneiss (Fig. 3). Work on Miocene to Pliocene basins in the Alaşehir–Gediz graben system (Çiftçi and Bozkurt 2009, 2010) has shown that this corrugation-like pattern also exists as basement topography in an axial direction of the Alaşehir–Gediz graben. This finding may support the hypothesis that ESE–WNW shortening was involved in controlling basin topography, which is also consistent with the observation that Miocene sediments onlap on folded orthogneiss (Purvis and Robertson 2005; Cemen et al. 2006).

The area north of Simav is a complex zone containing granitoids intrusions, ophiolitic klippen, volcanics and sediments. Magmatic activity related to Alpine convergence ranges from Eocene to Holocene in age with the largest volumes of igneous rocks produced during the Miocene (e.g. Ersoy et al. 2010). In general, there is a trend from older, subduction-related sub-alkaline magmatic compositions that intruded into the Izmir–Ankara zone in the north, to younger, alkaline compositions in the south (Seyitoglu and Scott 1996; Dilek and Altunkaynak 2009; Ersoy et al. 2010, Catlos et al. 2012). Oligocene–Miocene igneous activity took place in a post-collisional crustal extension setting and documents thermal melting of a previously metasomatized subcontinental lithospheric mantle (e.g. Prelević et al. 2012). Some of the granitoids, such as the Egrigöz granite, have intruded into the footwall of an extensional shear zone, defining at least part of the granite-intruded basement as a Miocene metamorphic core complex with ophiolitic

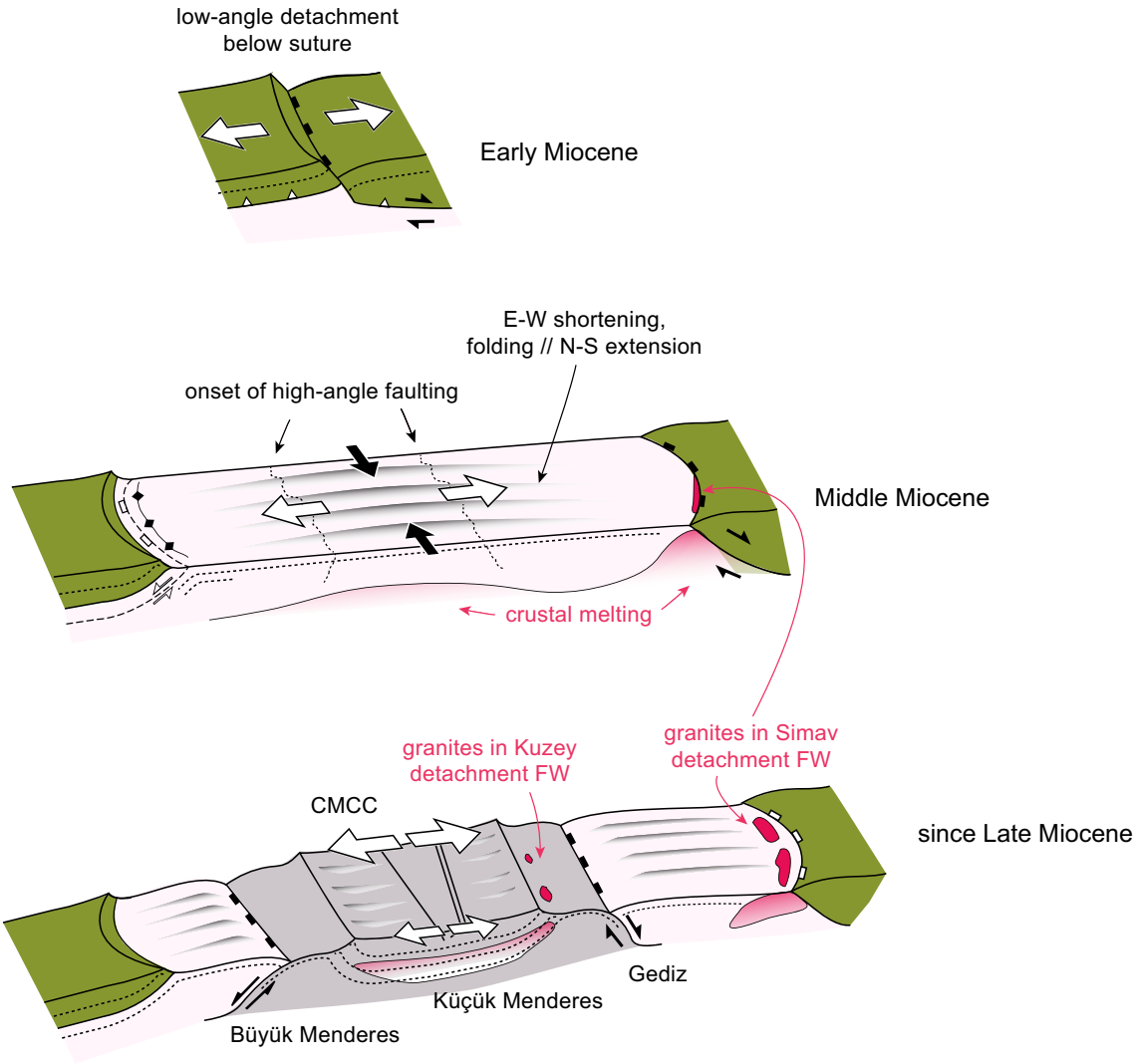

Fig. 2 Conceptual model of tectonic denudation of the Menderes Massif from the early Miocene to the present. Notice NNE-trending folds that formed parallel to stretching during to E–W shortening of basement in footwall of the early Miocene, Miocene crustal melts were exhumed soon after intrusion in the northern Menderes Massif, and further south, by the Kuzey detachment in the late Miocene

rocks of the Vardar–Izmir–Ankara zone in the hanging wall plate (e.g. Isik and Tekeli 2001; Ring and Collins 2005; Cemen et al. 2006). Although brittle deformation along the Simav fault zone may have originated in the early Miocene (Hetzel et al. 2013), its recent expression is a seismically active (Budakoğlu and Utkucu 2013) half-graben system (Toker 2014) with north-down normal sense displacement.

Previous geophysical studies

Western Anatolia has been the subject of a number of geophysical studies. Karabulut et al. (2013) used receiver functions from a temporary N–S deployment during the SIMBAAD passive seismic experiment (Salaün et al. 2012) to constrain crustal thickness at much higher resolutions than previous studies (e.g. Saunders et al. 1998; Sodoudi et al. 2006; Zhu et al. 2006) and showed that the Moho rises from c. 30 km in the northern Menderes Massif to c. 25 km in the south. Karabulut et al. (2013) report *Vp/Vs* ratios below 1.7 for the Bornova Flysch segment of the Vardar–Izmir–Ankara suture zone, which suggest an overall felsic crustal composition (Christensen 1996), whereas values in the Menderes Massif represent a more variable, intermediate composition that may become more mafic towards the south. For the northern Menderes Massif, Karabulut et al. (2013) also report a fabric of north-dipping velocity conversions. Magnetotelluric N–S profiles show a thick, highly conductive mid-crustal layer in the northern Menderes Massif that appears to become less intense and shallower towards the south, and image subvolcanic structures and basins (Bayrak

and Nalbant 2001; Gürer and Bayrak 2007; Ulugergerli et al. 2007). The Curie point depth has been constrained to levels of less than 20 km in the northern Menderes Massif and to less than 10 km in its central part (Aydın et al. 2005; Dolmaz et al. 2005; Bilim et al. 2016). In a large-scale study, Düzgit et al. (2006) have shown that gravity and magnetic anomalies display a long wavelength negative correlation across the Menderes Massif, which supports the proposal by above cited conductivity and Curie point depth studies that high heat flow and relatively thick crust of the Menderes Massif are due to asthenospheric upwelling.

Methodology

Data corrections

Data grids provided by Ariana Resources include maps of Bouguer gravity sampled every 1000 m and TMI aeromagnetic data sampled every 333 m. Each one of these data sets contains the geophysical response of structures seated at depths from the near surface up to the upper mantle, and, in the case of the aeromagnetic map, it also includes the geomagnetic field. The location of the inversion profiles was made based on a simplified lithological map derived from the 1:500,000 scale geological map of Turkey (Dubertret 1964) and by digital data provided by Ariana Resources (Fig. 3). To relate the gravity and magnetic signals to structures within the upper crust, the following corrections were applied to the gravity and magnetic data sets.

Bouguer gravity

Gravity data were assumed to be taken at ground level, and the proper elevation was assigned to the data from the digital elevation model provided. The Bouguer data contain a gradual trend of decreased gravity from the coastline

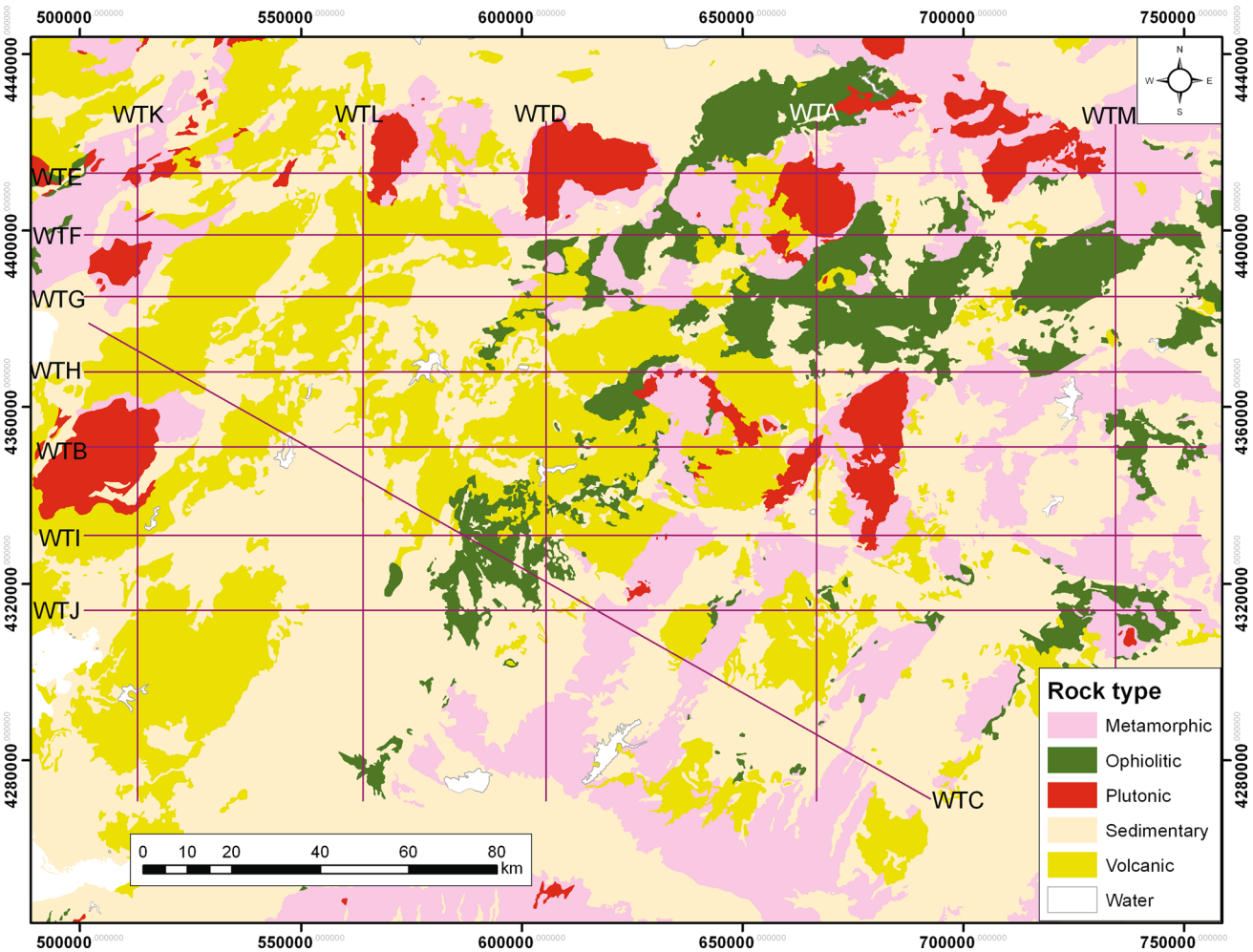

Fig. 3 Simplified lithological map of the study area in the northern Menderes Massif; volcanic units and granites refer to Miocene and younger magmatic activity; lines indicate location of profiles WTA–WTM

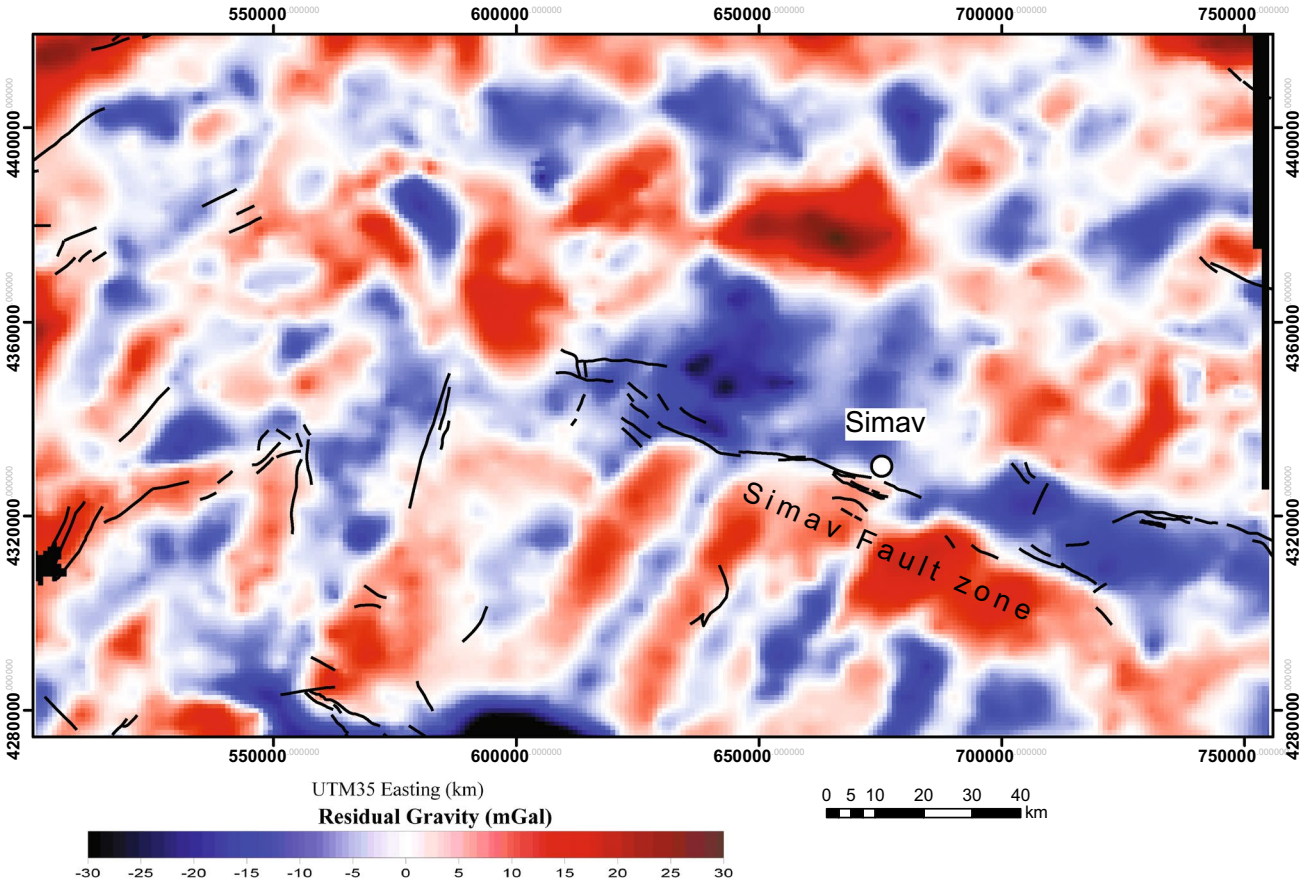

Fig. 4 Residual gravity anomaly map of study area with active faults shown for reference, including ESE-trending Simav fault zone in centre of map

towards the Anatolian plateau. This trend can be associated with expected variations in crustal thickness (Moho depths) in the area. Whereas this effect could have been removed by applying a wave number-based filter to the Bouguer data, we preferred to use the algorithm of Gallardo et al. (2005) to estimate variations in Moho depths. For this, we divided the area in a set of 5 km × 5 km vertical prisms and selected a compensation depth of 15 km along the coastline. We may expect that gravity effects due to heterogeneities above this compensation level would remain unaccounted for by this particular process and may match those heterogeneities that also produce a magnetic response, making them suitable for joint inversion. The gravity effect of the selected model of the Moho was then subtracted from the Bouguer data to produce the residual gravity anomaly (Fig. 4). These residual gravity data are deemed to represent mainly lateral variations in density above the Moho and, particularly, from the top 10 kilometres of the crust. It is noted, however, that resolution to shallow structures will be limited by the sampling rate of the original gravity data.

Aeromagnetic data

Aeromagnetic data were considered to be measured at a constant elevation of 2000 m above sea level. The data were subtracted from the geomagnetic field using the DGRF model for 1980 (e.g. Peddie 1982). The resulting magnetic anomaly (TMI) showed no regional trends as well as fully compensated positive and negative anomalies and was deemed suitable for joint inversion. To allow tracing profiles for joint inversion in multiple directions and to avoid the north–south phase shift associated with three-dimensional objects, the TMI magnetic anomaly was reduced to the pole obtaining the RTP anomaly (Fig. 5). This anomaly constitutes the magnetic information used for the joint inversion profiles. We extracted gravity and magnetic data from the gravity and magnetic grids along 13 profiles at grid resolutions and assigned precisions of 0.05 mGal for the gravity and 5 nT for the magnetic data. The precision on the gravity data is considered adequate for standard land surveys, whereas the precision of the

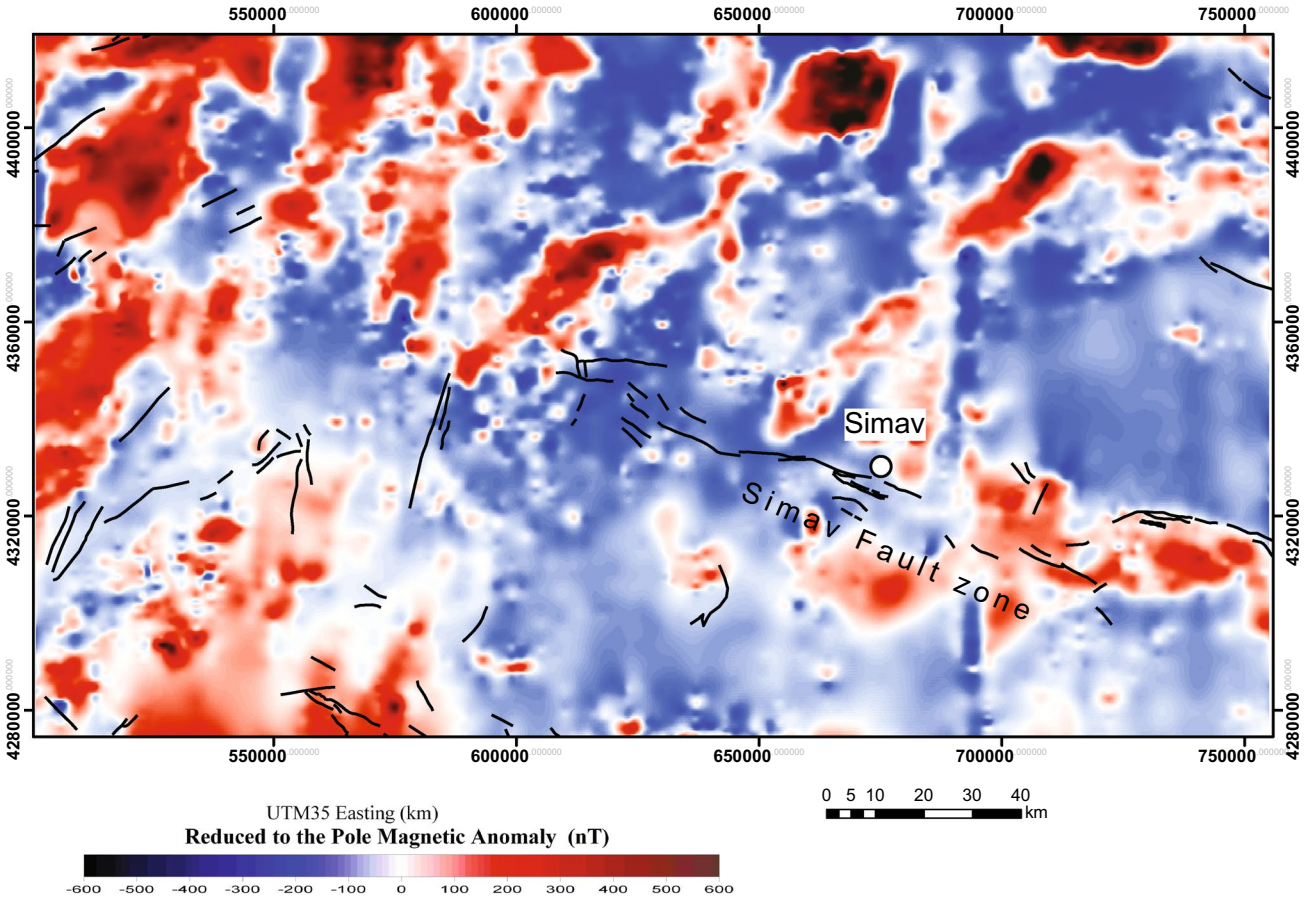

Fig. 5 Reduced to pole magnetic anomaly map of the study area with active faults shown for reference

magnetic data was considered appropriate due to the abundance of weakly magnetized bodies in large portions of the analysed sections.

Cross-gradient joint inversion

The theory of cross-gradient joint inversion can be found explained in detail in the literature (Gallardo 2007; Gallardo and Meju 2003; Gallardo and Meju 2004; Gallardo and Thebaud 2012). The aim is to simultaneously determine the subsurface distribution of different geophysical parameters, in our case density and magnetization, which should be structurally resembling and justify their corresponding geophysical data. The quantitative measure of structural resemblance is given by the cross-gradient function (Gallardo and Meju 2003), which observes the directional coincidence of collocated property changes regardless of the magnitude of the properties and the changes themselves. The acknowledged advantages of the cross-gradient joint inversion are that it (1) reduces the inherent model ambiguity that results when only one geophysical data type is inverted (2) finds correlated structures independently of the characteristic property values and structural attitude, which enables its application to multiple geological terrains, (3) facilitates an integrative structural interpretation by reconciling a unique structural framework straight from the multiple geophysical data together and (4) facilitates the identification and classification of different geological materials.

In our application, we used the algorithm of Gallardo (2007) as adapted to the joint inversion of gravity and magnetic data. The procedure of joint inversion starts with an initial (guess) model, which is changed through several iterative steps that gradually assimilate smaller scale features that are structurally resembling and whose geophysical responses reduce the mismatch to the observed geophysical data (cf. Gallardo and Meju 2013, Fig. 10). The used algorithm follows an overall sequence that is diagrammatically explicit in Gallardo et al. (2012, Fig. 5). Our specific processing was executed similar to the strategy followed in Gallardo and Thebaud (2012). We discretized the subsurface along the selected profile lines in rectangular

blocks 2000 m wide and between 100 and 500 m thick. The maximum studied depth was set to 10 km, and below this level the crust was assumed to be laterally homogenous in terms of density and magnetization. Differently to the case study in Gallardo and Thebaud (2012), which was located in an area of insignificant topography, much attention was set to the incorporation of the abrupt topography within the models. For this, 20 slabs of 100 m thickness were included on top of the sea level. The blocks above the local ground level were set density and magnetization contrasts of zero and were fixed during the inversion.

Various test experiments were conducted over a couple of profiles that cross distinct crustal domains in order to calibrate the process by determining the maximum level of smoothness that enables acceptable data fit while satisfying the structural resemblance imposed by the cross-gradient constraint. Once these parameters were selected, all studied profiles were processed with the same calibrated parameters.

Results

Gravity and magnetic anomaly curves, and the images of density and magnetization contrasts are shown as an example for profile WTA (Fig. 6) and in Supplement 1 for all remaining profiles. While these images can be interpreted conventionally by using the actual values provided, a more succinct analysis can be done by utilizing composed geospectral images (Figs. 6, 7) (Gallardo 2007). These images depict density and magnetization in a blended coloured scale projected on the red and green bands, as used in conventional radiometric or satellite imagery. In Supplement 2, we list the misfit between measured and modelled gravity and magnetic data.

Gravity map

The residual gravity anomaly map (Fig. 4) displays a strong NNE-trending stripy pattern with a wavelength between ca. 20 and 40 km that terminates at the ESE-trending Simav fault zone. North of the Simav fault zone the anomaly pattern is more chaotic and has a weak E–W component at a longer wavelength (ca. 50 km). The anomaly pattern is dominated by a large negative just north of the Simav fault zone and large positive to the north of the negative anomaly, both affecting the gravity field over an area on the order of c. 1500 km^2. In the western part of the study area, the NNE pattern is still visible, but it is not as clear as in the southern part and appears disrupted by anomalies in various orientations. When the residual gravity anomaly map is compared to the lithological map (Fig. 3), gravity highs correlate with orthogneiss-rich basement lithologies and ultramafic-rich ophiolitic units, and lows with granitic intrusions, volcanics and sedimentary basins.

Fig. 6 Results of the cross-gradient joint inversion for profile WTA, including anomaly curves (**a**), geospectral image (**b**), corresponding profiles for contrasts of density (**c**) and magnetization (**d**); notice negative correlation between magnetic and gravity anomalies from 95 to 125 km and from 125 to 150 km; (**e**) shows schematic template for interpreting profiles according to cross-gradient inversion *colour* space ('geospectral image') as used in (**b**) and in the geospectral images shown in following figures; (**f**) and (**g**) show anomaly *curves* and geospectral image of profile WTK; (**h**) and (**i**) respective data for profile WTM; see Fig. 3 for location of profiles

Magnetic anomaly map

The reduced to the pole magnetic anomaly map (Fig. 5) shows a pattern of positive anomaly ridges to the north and the west of the Simav fault zone. The positive anomaly ridges increase in width from east to west and have a weak NE trend. The area south of the Simav fault zone is generally negative, except for a positive area at its eastern end, and a wide positive area in the southwest of the study area. When compared to lithology (Fig. 3), the magnetic anomaly pattern shows that granitoid intrusions correlate well with magnetic highs, while the remaining rock types are generally negative. Particularly in the northwest of the study area, positive anomalies extend over much wider areas than granites in outcrop, suggesting a larger subsurface extent of either volcanic cover, or the intrusions. A north–south-oriented linear feature around 708880E is likely to represent an artefact along the stitching lines of the primary data sets.

Profiles

Thirteen profiles were produced from the gravity and magnetic data provided by Ariana Resources, using the cross-gradient joint inversion algorithm of Gallardo (2007). Density and magnetization values for these profiles are combined in 'geospectral' images (Fig. 6a–e) (Gallardo 2007) using a colour scheme that takes into account the range of density and magnetization variations found for the profiles (Fig. 6c, d). Specific ranges of values in gravity–magnetization for each section vary according to the distribution of their specific anomalies. However, for an integrated analysis, we selected a common colour scale that favours the visualization of the more abundant low magnetized bodies. A simplified template that suggests a possible correlation of the coupled density–magnetization contrast to lithology is shown as Fig. 6e. The relative sampling abundance of different density–magnetization clusters is shown in the ensemble of cross-plots in Supplement 3.

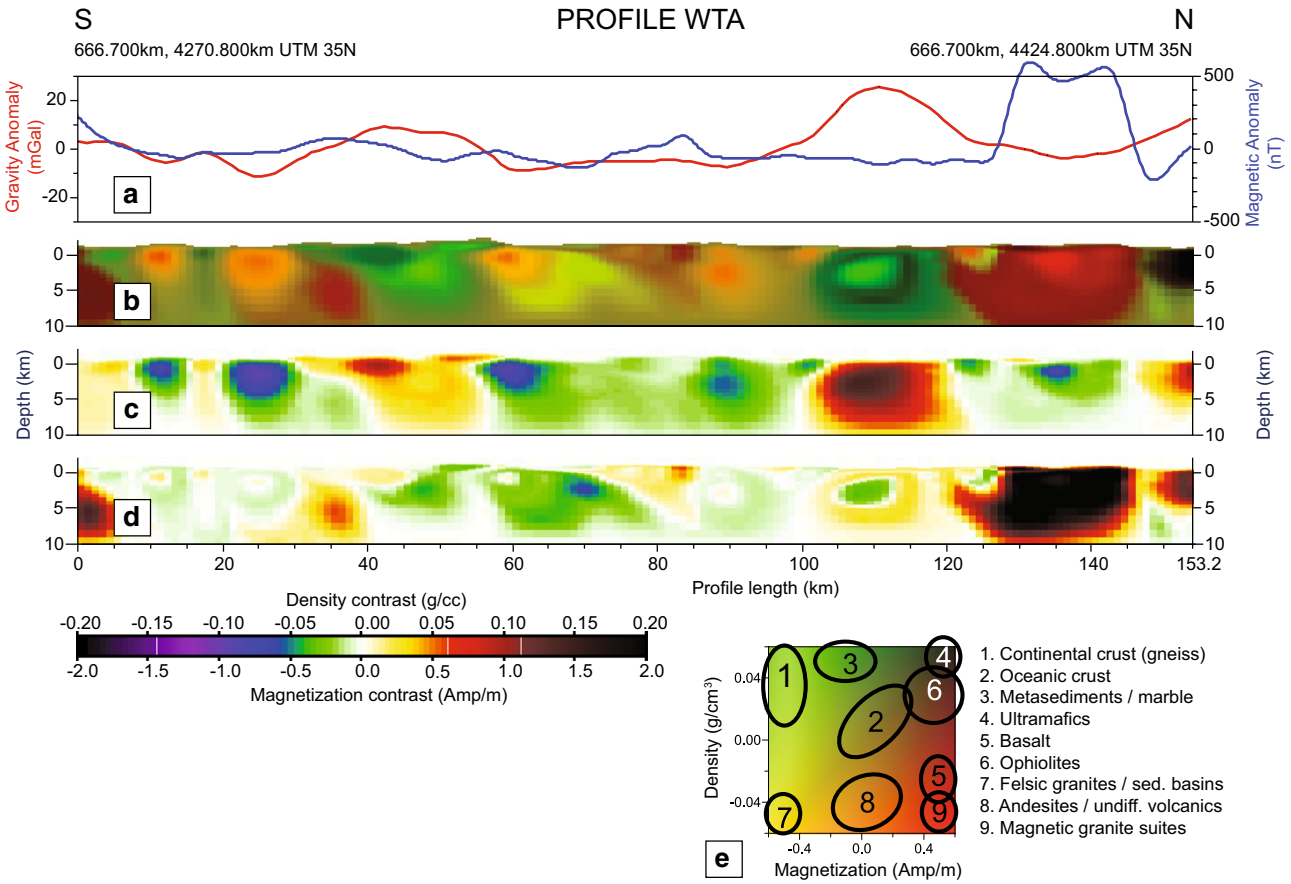
S
PROFILE WTA
N
666.700km, 4270.800km UTM 35N
666.700km, 4424.800km UTM 35N
Gravity Anomaly (mGal)
Magnetic Anomaly (nT)
Depth (km)
Profile length (km)
Density contrast (g/cc)
Magnetization contrast (Amp/m)
Density (g/cm-3)
Magnetization (Amp/m)
1. Continental crust (gneiss)
2. Oceanic crust
3. Metasediments / marble
4. Ultramafics
5. Basalt
6. Ophiolites
7. Felsic granites / sed. basins
8. Andesites / undiff. volcanics
9. Magnetic granite suites

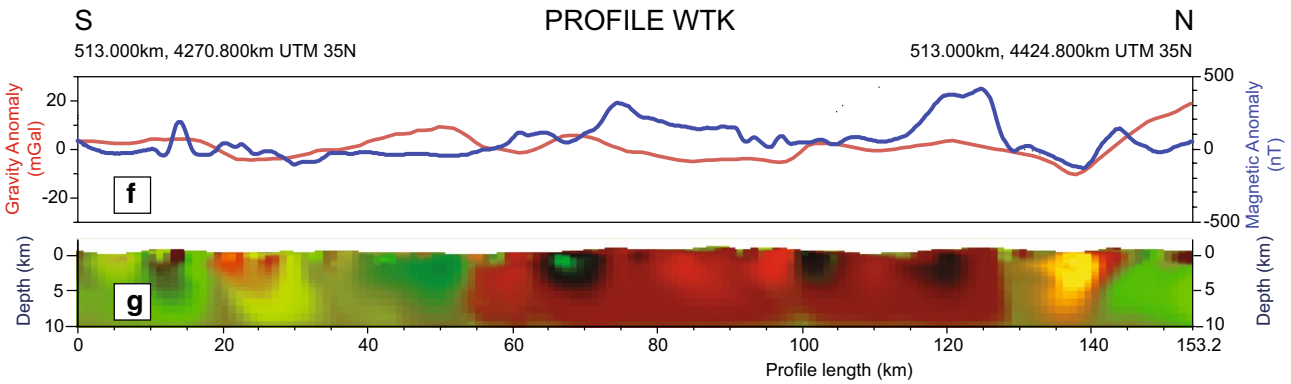
S
PROFILE WTK
N
513.000km, 4270.800km UTM 35N
513.000km, 4424.800km UTM 35N
Gravity Anomaly (mGal)
Magnetic Anomaly (nT)
Depth (km)
Profile length (km)

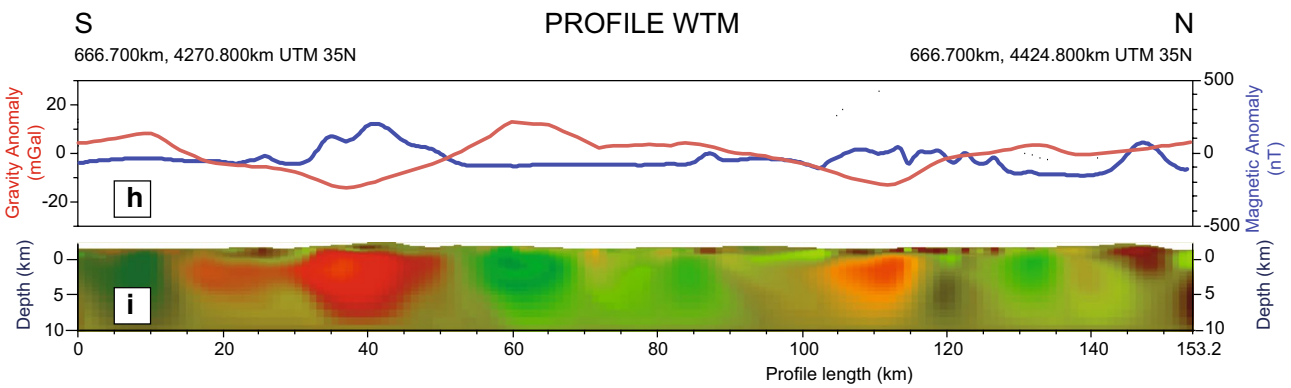
S
PROFILE WTM
N
666.700km, 4270.800km UTM 35N
666.700km, 4424.800km UTM 35N
Gravity Anomaly (mGal)
Magnetic Anomaly (nT)
Depth (km)
Profile length (km)

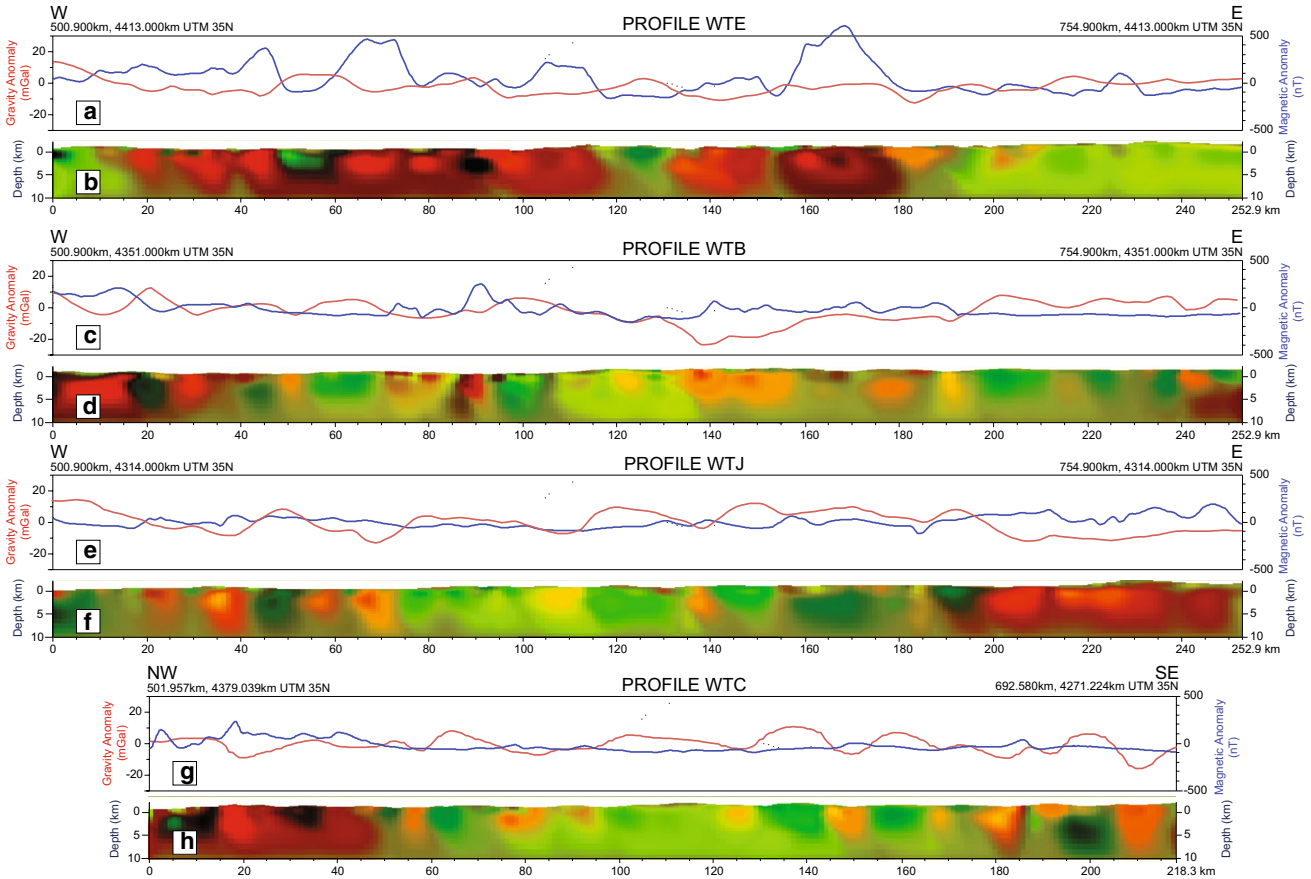

Fig. 7 Results of the cross-gradient joint inversion including anomaly curves and geospectral images for profiles WTE (**a**, **b**), WTB (**c**, **d**), WTJ (**e**, **f**) and WTC (**g**, **h**)

For the sake of brevity, we outline the salient features of the inversion study using seven exemplary profiles, three in N–S orientation (WTA, WTK and WTM; Fig. 6), three in E–W orientation (WTE, WTB, WTJ; Fig. 7a–f) and one oriented ESE–WNW (WTC; Fig. 7g, h). The geospectral images of all sections are shown at their location in a summary map (Fig. 8). For profile WTA, we show the detailed gravity and magnetic anomaly curves, the geospectral image and its density and magnetization profiles in detail (Fig. 6a–e). For the remaining sections in Figs. 6 and 7, we focus on the anomaly curves and the geospectral images only. The detailed sections including density and magnetization profiles can be accessed as Supplement 1.

In general, the profiles reveal two main crustal zones: a zone of high density and low magnetization in the centre of the area in light green to yellow colours in the geospectral images. In contrast, red, dark green and black colours dominate the less dense but highly magnetized zone in the north, west and to the east.

North–south profiles

Profile WTA (Fig. 6a–d) is N–S oriented and located east of the centre of the study area (Fig. 3). The distribution of density heterogeneities estimated by the cross-gradient joint inversion displays an overall north-dipping trend, except near two heterogeneities in the northern third of the section. These heterogeneities are a density high and a magnetization high (respectively, from c. 95–125 km and c. 125–150 km; in Fig. 6a, b), each of which correlates with a flat response in the other potential field over the same range. The gravity high relates spatially to a wide outcrop area of ophiolite, while the magnetic high relates to a nearby granitoid intrusion. The Egrigöz intrusion near c. 80 km has a weaker magnetic anomaly, while the juxtaposition of metamorphic rocks with sedimentary rocks along the Simav Fault zone at c. 58 km is clearly detected. Two negative gravity anomalies at the southern end of the section are likely to be related to volcanic edifices.

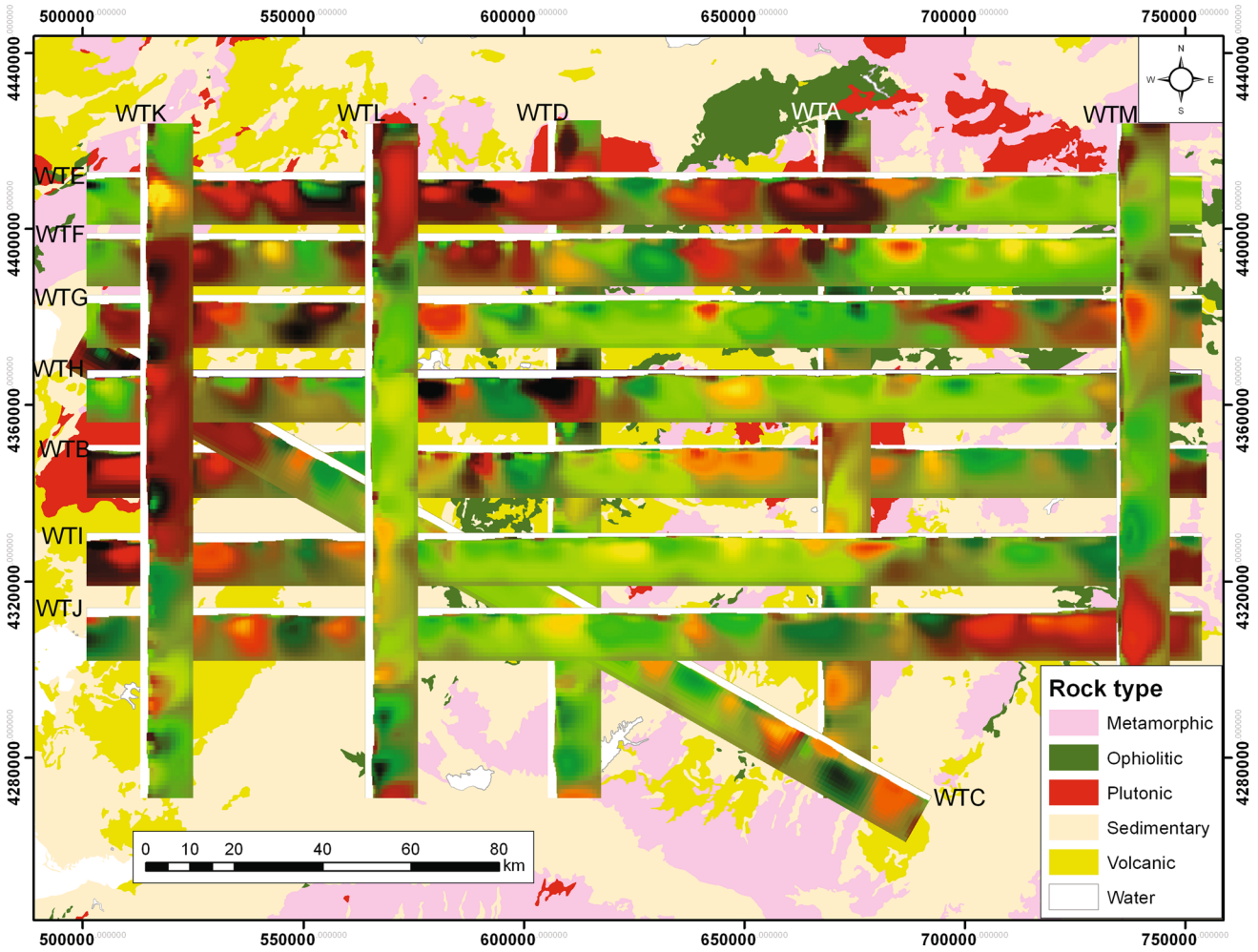

Fig. 8 Geospectral images overlain onto simplified lithology; notice correlation of magnetic highs with gravity lows—depicted in red in the geospectral images—around Miocene granitoid intrusions in the north, the west and the southeast of the study area

Profile WTK (Fig. 6f, g) is oriented N–S and is located in the west of the study area. This profile has a relatively flat, low-amplitude gravity anomaly pattern, but shows a relatively wide magnetic high in the centre of the section (c. 55–130 km). South of this large magnetic high, the gravity and magnetic anomalies are relatively flat, with gravity undulating at wavelengths of about 20–25 km. North of the positive magnetic anomaly, both values drop to a sharp and very low trough, before gravity increases steadily and magnetic values start to undulate. In this section, it is difficult to properly define accretionary and continental crust domains, and the northern end's spectra appear to be atypical compared to other areas, probably because north of 140 km a distinctly different tectonic unit, the Sakarya zone (Fig. 1), would be expected.

Profile WTM (Fig. 6h, i) is oriented N–S and is located close to the eastern boundary of the study area. The profile is dominated by a coincident gravity low and magnetic high between 30 and 50 km and a similar pattern of lesser amplitude between 100 and 120 km. The high density plus low magnetization that is typical for the metamorphic basement-dominated area is only observed between 50 and 100 km and from 125 to 145 km. The northern end is likely to be part of the subduction–accretion complex.

East–west profiles

Profile WTE (Fig. 7a, b) is oriented E–W and located in the northern part of the study area (Fig. 3). The cross-gradient joint inversion shows the strongest magnetic heterogeneities for the whole area in the west; non-magnetic responses can be found to the east (km 195 onwards). Gravity anomalies are generally negative in the east and are averaged to zero in the west (Fig. 7a). This division is common between the subduction–accretion complex (e.g. west of km 195) and continental crust (e.g. east of km 195).

The western portion of WTE shows an alternation of low-density magnetic units—likely related to major

intrusion—with denser non-magnetic units coloured olive to dark green. Intrusions depicted in intense red around km 5, km 82–87, km 110 are less dense at km 160–180 depicted in darker red probably following a change in composition. Major blocks of denser non-magnetic units in dark green found, for instance, at position km 50–60 km, km 120–130 seem related to metacarbonates (marbles) or metasediments. Very dark colours (black) represent very dense and very magnetic units, near the 90 km mark. Two possible explanations for this combination are the existence of ultramafic units, or basic volcanic complexes overlying a denser crust of metasediments or a localized magnetic intrusive hosted within denser metasedimentary crust. Ophiolitic complexes in olive green to reddish-green seem present around km 155–195 where they are intruded and possibly between km 120 to 140 at the flanks of metasedimentary crust. Orange units at km 140 and km 182 may represent intermediate volcanic deposits. Structural attitude in this area is generally east dipping.

Characteristic for the continental crust domain is bright green colours that are likely to represent gneiss or non-magnetic metasediments, and yellow to orange colours near the 220 km mark and east of 240 km (Fig. 7b). Lighter colours may relate to local basins filled with either sediments or non-magnetic volcanics. Red colour tones are characteristic of ultramafic rocks in ophiolitic units, which are present as a thin layer between 215 and 233 km, and in thicker quantities at depth between 225 and 230 km. Structural attitude for the continental crust domain shows no dipping trend.

Profile WTB (Fig. 7c, d) extends from west to east across the centre of the study area (Fig. 3). The cross-gradient joint inversion pattern is noisy in the west and quieter in the east (Fig. 7d). Gravity highs are relatively low amplitude and occur at ca. 20, 40, 100 km and between 195 and 240 km. The gravity highs apparently relate to metamorphic basement (20 km), carbonate sediments (40 km), ophiolitic rocks (100 km) and a combination of ophiolitic rocks and metamorphic basement rocks in the east, whereas relatively short wavelength gravity lows occur at 30, 50 and 80 km; a wide and variable negative anomaly is visible between 110 and 195 km. The latter anomaly relates well to a combination of granitoid intrusions and volcanics (Fig. 3), whereas the former appears to relate to volcanics only. A pronounced magnetic high is visible from 0 to 20 km; a very strong, short wavelength high at 90 km; and small anomaly peaks between ca. 135 and 190 km. The magnetic anomalies appear to relate to a granitoid intrusion in the west (0–20 km), a small but distinct volcanic unit at 90 km, and to the same combination of volcanics and granitoids that cause the gravity low between 110 and 195 km (Fig. 3).

In the E–W profile WTJ (Fig. 7e, f), the western part shows higher magnetization combined with variable gravity and similar to WTE and WTB a relatively quiet central area characterized by a more consistent gravity anomaly ‘plateau’, coincident with relatively low magnetic anomaly values. The surprising feature, however, is a large gravity low and magnetic high east of c. 195 km. This pattern likely indicates a large intrusive or subvolcanic rock mass.

Profile WTC

Profile WTC (Fig. 7g, h) is oriented WNW–ESE across the SE quadrant of the study area (Fig. 3) perpendicular to the Miocene to recent stretching of the Menderes Massif (Fig. 1). The pattern in the cross-gradient joint inversion image is noisy in the west and quieter in the remaining area. Between c. 65 and 130 km, the upper ca. 1–2 km shows a markedly noisier pattern compared to the region below. This could be due to a relatively thin volcanic cover. The gravity anomaly pattern shows a 20–40 km wavelength alternation between highs and lows. These highs can largely be attributed to metamorphic basement and ophiolitic rocks, while occurrences of granitoids, volcanic and sedimentary rocks relate well to gravity lows. The magnetic anomaly pattern is noisy at the west end, but otherwise remarkably quiet, including a low magnitude, but wide low that extends from 60 to 180 km. The magnetic high at the west end overall correlates well with a granitoid intrusion, but it is not clear why there are such big variations in this domain. The low in the centre of the profile is spatially related to the metamorphic basement and the locally overlying basins.

Discussion

Imaging the composition and structure of the upper crust in the northern Menderes Massif with cross-gradient joint inversion of gravity and magnetic data has produced valuable information that is complementary to and largely independent of geological and petrophysical data. The produced geospectral profiles provide a first-order assessment of crustal structure across a complexly deformed portion of the Tethyan orogen, and when placed on a geological map they not only show many similarities with mapped and geological units mapped at the surface (Fig. 8), but also provide information on their depth extent. Our inversion technique provides valuable constraints on the extent of Miocene to recent basins and on exposed and buried magmatic bodies (Fig. 9) that may be of interest for mineral and energy resource exploration.

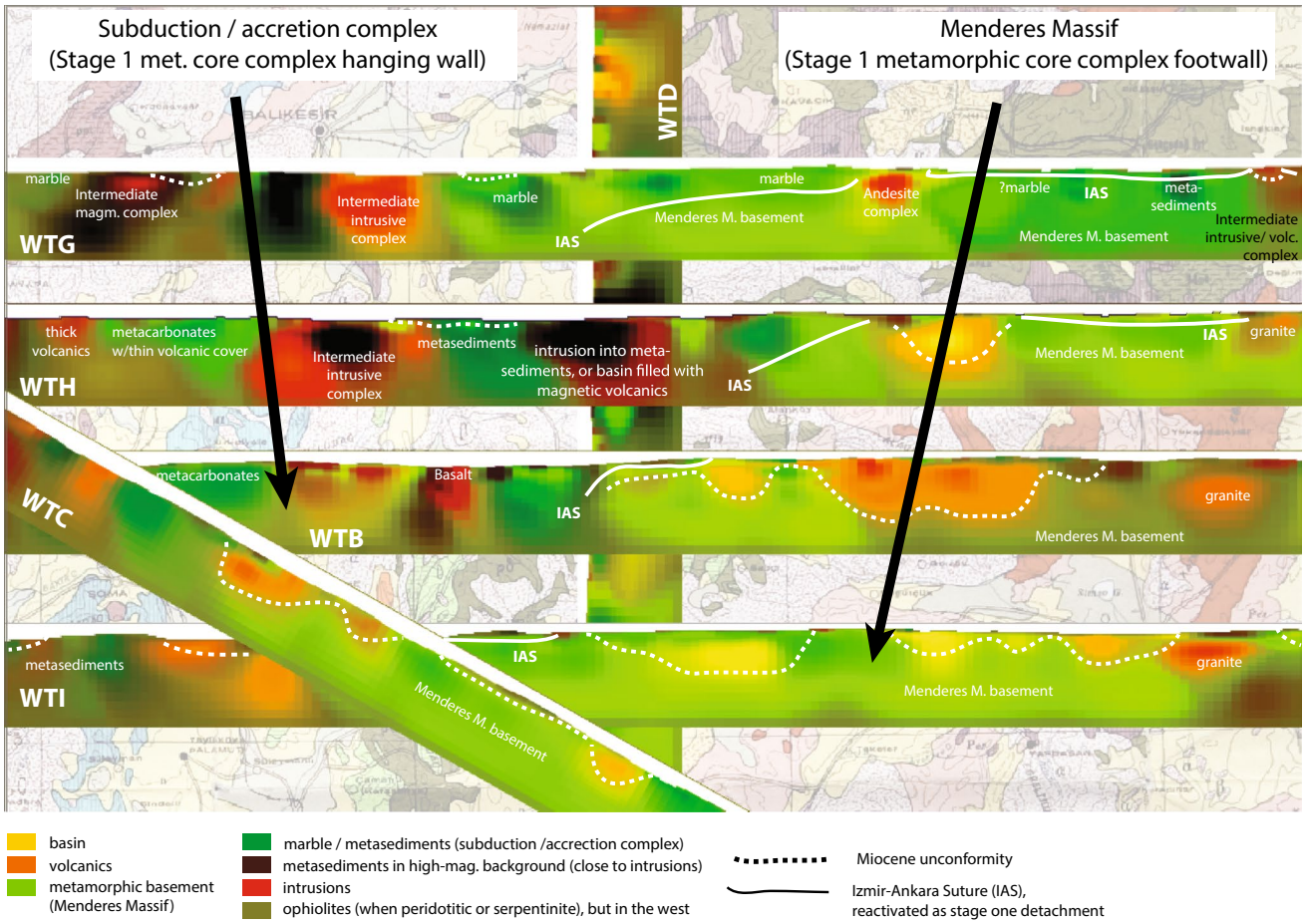

Fig. 9 Interpretation of the central portion of the study area with parts of profiles WTG, WTH, WTC, WTB and WTI, including our interpretation of the Miocene unconformity and the Vardar–Izmir–Ankara suture zone; background is 1:500,000 Geological Map of Turkey (Dubertret 1964)

Lithology and tectonic stratigraphy

We correlate lithology to geophysical response based on colours of the geospectral images in the study area (Figs. 6, 7, 8). Two distinctive crustal domains can be seen in all sections, one that is more magnetic with variable, but often overall lower density ('olive' coloured matrix), and one that is more dense with variable but generally lower magnetization (bright green matrix/background in the central and eastern central part).

We interpret these domains with different crustal compositions as terranes, the subduction–accretion complex of the Izmir–Ankara portion of the Vardar–Izmir–Ankara suture zone, and the continental crust of the Anatolian microcontinent. Whereas the subduction–accretion complex occurs in thin klippen in the centre and east, it makes up the entire studied depth of the crust in the west and possibly in the southeast. This characterization of the subduction–accretion complex is consistent with the presence of thick, highly conductive layers in the crust imaged by magnetotelluric studies (Bayrak and Nalbant 2001; Gürer and Bayrak 2007; Ulugergerli et al. 2007). A north-dipping 'fabric' of contrasting material is a striking characteristic in the central section WTA (Fig. 6) and is similar to north-dipping feature that was imaged in the northern Menderes Massif by passive seismic (Karabulut et al. 2013) and magnetotelluric (Ulugergerli et al. 2007) methods.

Intrusions show up as more magnetic granites (red), or as mafic intrusives or volcanics (dark red) in the subduction–accretion complex, but appear to be less magnetic (orange) in the continental crust of the Anatolian microcontinent. The distinct low *Vp/Vs* ratio (<1.7) imaged by Karabulut et al. (2013) for the northern Bornova Flysch zone, which roughly coincides with NW portion of the study area, may be the result of large volumes of slow felsic magma that have intruded the dense and fast mafic rocks of the subduction–accretion complex as for example suggested by the western end of section WTE (Fig. 7).

Miocene basins contain sedimentary rocks (yellow), felsic volcanics (orange) or mafic volcanics (red to black).

The shape of the basins is mostly as a simple syncline type. Although our method images the location of the basins quite well, the depth is probably slightly overestimated as the smoothness imposed in the cross-gradient constraint favours smaller property contrast distributed in larger volumes. We do, however, prefer this approach as it provides moderate estimates of property distributions and is less prone to enhance sharp model artefacts. The Simav basin, for example, is imaged around the 60-km profile length mark to a depth of at least 2 km, whereas Toker (2014) in a more detailed gravity and magnetic anomaly study has estimated a bedrock depth of 1–1.2 km.

The overall stratigraphy is as follows: the lowest tectonic unit consists of metamorphic lithologies—imaged in bright green in the geospectral images—of the Menderes nappes as exposed across the Menderes Massif (Gessner et al. 2001a, 2004, 2013). The Menderes nappes are overlain by the subduction–accretion complex of the Bornova Flysch, Tavşanli and Afyon zones consisting of mafic magmatic rocks of the oceanic crust and Mesozoic sediments, which in parts are metamorphosed. Miocene to recent sedimentary basins occur on both the subduction–accretion and the metamorphic basement domains.

Tectonic implications

The boundary between the subduction–accretion complex and the continental crust of the Anatolian microcontinent can be tracked or inferred from the sections and in general fits well with the exposed rocks. Whereas in the west and in the north the subduction–accretion complex makes up the entire depth of the investigated upper crust, it only occurs in thin sheets in the centre and to the east of the northern Menderes Massif and the southeast of the study area. The boundary is a steep structure in the west and a shallowly dipping structure in the centre of the area. Where shallow, the boundary is likely to be an extensional detachment that reactivated the original Eocene–Oligocene Neotethyan suture thrust, as large parts of the orogenic stack are missing between the ophiolite and the Menderes nappes (Gessner et al. 2013, and references therein). Whereas granites and volcanic complexes are interspersed across the study area, they are much more numerous in the west. In the central part, the volcanics and basins directly overly the gneissic basement, which suggests that the subduction complex has been tectonically removed or eroded. The deepening of the subduction–accretion complex detected by the inversion profiles is in agreement with the proposal by Gessner et al. (2013) that the West Anatolia Transfer Zone is the western limit of the Anatolian microcontinent. From the limited resolution of our investigation, we cannot, however, shed further light on the question where igneous activity in the northern Menderes Massif post-dates extensional detachment faults (Akay 2009; Catlos et al. 2012). Our results show the potential for further, more detailed 'structural geophysics' research to test conceptual models of local geological features.

Conclusions

We used cross-gradient joint inversion of gravity and magnetic data to image and characterize the structure and composition of Earth's upper crust in the northern Menderes Massif in western Anatolia. Applying the cross-gradient joint inversion method allows us to better define the subsurface geology of the northern Menderes Massif. Our results are in overall agreement with interpretations based on geological mapping and structural analysis, and we are able to trace the regional stratigraphy and tectonic boundaries such as the West Anatolia Transfer Zone and the Vardar–Izmir–Ankara suture zone based on potential field data.

Acknowledgments We acknowledge financial support by Ariana Resources plc. Vanessa Markwitz is thanked for comments of an earlier version; reviews by Nuri Dolmaz and an anonymous reviewer helped to improve the manuscript. Klaus Gessner, now with the Geological Survey of Western Australia, publishes in the role of Adjunct Senior Research Fellow at the Centre for Exploration Targeting, University of Western Australia.

References

Akay E (2009) Geology and petrology of the Simav Magmatic Complex (NW Anatolia) and its comparison with the Oligo-Miocene granitoids in NW Anatolia: implications on Tertiary tectonic evolution of the region. Int J Earth Sci 98(7):1655–1675

Aydın İ, Karat Hİ, Koçak A (2005) Curie-point depth map of Turkey. Geophys J Int 162(2):633–640

Bayrak M, Nalbant S (2001) Conductive crust imaged in western Turkey by MT. Geophys Res Lett 28(18):3521–3524

Bilim F, Akay T, Aydemir A, Kosaroglu S (2016) Curie point depth, heat-flow and radiogenic heat production deduced from the spectral analysis of the aeromagnetic data for geothermal investigation on the Menderes Massif and the Aegean Region, western Turkey. Geothermics 60:44–57

Budakoğlu E, Utkucu M (2013) 19 Mayis 2011 Simav depreminin uzak-alan kayitlariyla incelenmesi (in Turkish). In: 2nd Turkish earthquake engineering and seismology conference (2 Türkiye Deprem Mühendisliği ve Sismoloji Konferansı), Hatay, Turkey, pp 1–6

Candan O, Dora OÖ, Oberhänsli R, Çetinkaplan M, Partzsch JH, Warkus FC, Dürr S (2001) Pan-African high-pressure metamorphism in the Precambrian basement of the Menderes Massif, western Anatolia, Turkey. Int J Earth Sci (Geologische Rundschau) 89:793–811

Candan O, Koralay OE, Akal C, Kaya O, Oberhänsli R, Dora OÖ, Konak N, Chen F (2011) Supra-Pan-African unconformity between core and cover series of the Menderes Massif/Turkey and its geological implications. Precambr Res 184(1–4):1–23. doi:10.1016/j.precamres.2010.09.010

Catlos EJ, Çemen I (2005) Monazite ages and the evolution of the Menderes Massif. Int J Earth Sci 94(2):204–217

Catlos E, Jacob L, Oyman T, Sorensen S (2012) Long-term exhumation of an Aegean metamorphic core complex granitoids in the Northern Menderes Massif, western Turkey. Am J Sci 312(5):534–571. doi:10.2475/05.2012.03

Cemen I, Catlos EJ, Gögüs O, Özerdem C (2006) Postcollisional extensional tectonics and exhumation of the Menderes massif in the Western Anatolia extended terrane, Turkey. In: Dilek Y, Pavlides S (eds) Postcollisional tectonics and magmatism in the Mediterranean region and Asia. Geological Society of America Special Paper 409, pp 353–379

Christensen NI (1996) Poisson's ratio and crustal seismology. J Geophys Res B Solid Earth 101:3139–3156

Çiftçi NB, Bozkurt E (2009) Evolution of the Miocene sedimentary fill of the Gediz Graben, SW Turkey. Sediment Geol 216(3–4):49–79. doi:10.1016/j.sedgeo.2009.01.004

Çiftçi NB, Bozkurt E (2010) Structural evolution of the Gediz Graben, SW Turkey: temporal and spatial variation of the graben basin. Basin Res 22(6):846–873. doi:10.1111/j.1365-2117.2009.00438.x

Cohen HA, Dart CJ, Akyüz HS, Barka A (1995) Syn-rift sedimentation and structural development of the Gediz and Büyük Menderes graben, western Turkey. J Geol Soc Lond 152:629–638

Dilek Y, Altunkaynak Ş (2009) Geochemical and temporal evolution of Cenozoic magmatism in western Turkey: mantle response to collision, slab break-off, and lithospheric tearing in an orogenic belt. In: Van Hinsbergen DJJ, Edwards MA, Govers R (eds) Collision and collapse at the Africa–Arabia–Eurasia subduction zone. The Geological Society, London, Special Publication 311, London

Dolmaz M, Hisarli Z, Ustaömer T, Orbay N (2005) Curie point depths based on spectrum analysis of aeromagnetic data, West Anatolian extensional province, Turkey. Pure appl Geophys 162(3):571–590

Dubertret L (1964) Geological Map of Turkey, 1:500,000 series Izmir sheet. Maden Tetkik ve Arama Enstitüsü, Ankara

Düzgit Z, Hisarli ZM, Sayin N, Orbay N (2006) Correlation between gravity and magnetic anomalies of Western Anatolia and its relation to tectonic structures. Earth Planets Space 58(8):943–949

Emre T, Sözbilir H (2007) Tectonic evolution of the Kiraz Basin, Küçük Menderes Graben: evidence for compression/uplift-related basin formation overprinted by extensional tectonics in West Anatolia. Turk J Earth Sci 16:441–470

Erkül F (2010) Tectonic significance of synextensional ductile shear zones within the Early Miocene Alaçamdag granites, northwestern Turkey. Geol Mag 147:611–637

Ersoy EY, Helvacı C, Palmer MR (2010) Mantle source characteristics and melting models for the early-middle Miocene mafic volcanism in Western Anatolia: implications for enrichment processes of mantle lithosphere and origin of K-rich volcanism in post-collisional settings. J Volcanol Geotherm Res 198(1–2):112–128

Faulds JE, Bouchot V, Moeck I, Oguz K (2009) Structural controls on geothermal systems in western Turkey: a preliminary report. Geotherm Resour Counc Trans 33:375–381

Gallardo LA (2007) Multiple cross-gradient joint inversion for geospectral imaging. Geophys Res Lett 34(19):L19301

Gallardo LA, Meju MA (2003) Characterization of heterogeneous nearsurface materials by joint 2D inversion of dc resistivity and seismic data. Geophys Res Lett 30(13):1658–1661

Gallardo LA, Meju MA (2004) Joint two-dimensional DC resistivity and seismic travel time inversion with cross-gradients constraints. J Geophys Res Solid Earth 109(B3):B03311. doi:10.1029/2003JB002716

Gallardo LA, Meju MA (2011) Structure-coupled multiphysics imaging in geophysical sciences. Rev Geophys 49(1):1–19

Gallardo LA, Thebaud N (2012) New insights into Archean granite-greenstone architecture through joint gravity and magnetic inversion. Geology 40(3):215–218. doi:10.1130/g32817.1

Gallardo LA, Perez-Flores MA, Gomez-Trevino E (2005) Refinement of three-dimensional multilayer models of basins and crustal environments by inversion of gravity and magnetic data. Tectonophysics 397:37–54

Gallardo LA, Fontes SL, Meju MA, Buonora MP, de Lugao PP (2012) Robust geophysical integration through structure-coupled joint inversion and multispectral fusion of seismic reflection, magnetotelluric, magnetic, and gravity images: example from Santos Basin, offshore Brazil. Geophysics 77(5):B237–B251. doi:10.1190/geo2011-0394.1

Gessner K, Ring U, Johnson C, Hetzel R, Passchier CW, Gungor T (2001a) An active bivergent rolling-hinge detachment system: Central Menderes metamorphic core complex in western Turkey. Geology 29:611–614

Gessner K, Piazolo S, Gungor T, Ring U, Kroener A, Passchier CW (2001b) Tectonic significance of deformation patterns in granitoid rocks of the Menderes nappes, Anatolide Belt, Southwest Turkey. Int J Earth Sci 89:766–780

Gessner K, Ring U, Passchier CW, Gungor T (2001c) How to resist subduction: evidence for large-scale out-of-sequence thrusting during Eocene collision in western Turkey. J Geol Soc 158:769–784

Gessner K, Collins AS, Ring U, Gungor T (2004) Structural and thermal history of poly-orogenic basement: U–Pb geochronology of granitoid rocks in the southern Menderes Massif, Western Turkey. J Geol Soc 161:93–101

Gessner K, Gallardo LA, Markwitz V, Ring U, Thomson SN (2013) What caused the denudation of the Menderes Massif: review of crustal evolution, lithosphere structure, and dynamic topography in southwest Turkey. Gondwana Res 24:243–274

Glodny J, Hetzel R (2007) Precise U–Pb ages of syn-extensional Miocene intrusions in the central Menderes Massif, western Turkey. Geol Mag 144(2):235–246

Gürer A, Bayrak M (2007) Relation between electrical resistivity and earthquake generation in the crust of West Anatolia, Turkey. Tectonophysics 445(1):49–65

Haber E, Gazit MH (2013) Model fusion and joint inversion. Surv Geophys 34:675–695

Hancock PL, Barka AA (1987) Kinematic indicators on active normal faults in western Turkey. J Struct Geol 9(5/6):573–584

Hetzel R, Reischmann T (1996) Intrusion age of Pan-African augen gneisses in the southern Menderes massif and the age of cooling after Alpine ductile extensional deformation. Geol Mag 133:565–572

Hetzel R, Passchier CW, Ring U, Dora OÖ (1995a) Bivergent extension in orogenic belts: the Menderes massif, southwestern Turkey. Geology 23:455–458

Hetzel R, Ring U, Akal C, Troesch M (1995b) Miocene NNE-directed extensional unroofing in the Menderes massif, southwestern Turkey. J Geol Soc 152:639–654

Hetzel R, Zwingmann H, Mulch A, Gessner K, Akal C, Hampel A, Güngör T, Petschick R, Mikes T, Wedin F (2013) Spatiotemporal evolution of brittle normal faulting and fluid infiltration in detachment fault systems: a case study from the Menderes Massif, western Turkey. Tectonics 32(3):364–376

Isik V, Tekeli O (2001) Structure of lower plate rocks in metamorphic core complex: Northern Menderes Massif, Western Turkey. Int J Earth Sci (Geologische Rundschau) 89:757–765

Karabulut H, Paul A, Ergün TA, Hatzfeld D, Childs DM, Aktar M (2013) Long-wavelength undulations of the seismic Moho beneath the strongly stretched Western Anatolia. Geophys J Int 194(1):450–464

Kröner A, Sengör AMC (1990) Archean and Proterozoic ancestry in late Precambrian to early Proterozoic crustal elements of

southern Turkey as revealed by single-zircon dating. Geology 18:1186–1190
Makris J, Stobbe C (1984) Physical properties and state of the crust and upper mantle of the Eastern Mediterranean Sea deduced from geophysical data. Mar Geol 55:347–363
Mutlu AK, Karabulut H (2011) Anisotropic Pn tomography of Turkey and adjacent regions. Geophys J Int 187(3):1743–1758. doi:10.1111/j.1365-246X.2011.05235.x
Oberhänsli R, Candan O, Wilke F (2010) Geochronological evidence of Pan-African eclogites from the central Menderes Massif, Turkey. Turk J Earth Sci 19(4):431–447
Okay AI (2010) Deep subduction of a passive continental margin: comparison of the Tavsanli zone and Oman. In: Tectonic crossroads: evolving orogens of Eurasia–Africa–Arabia, Ankara, pp 36. https://gsa.confex.com/gsa/2010TU/finalprogram/abstract_175096.htm
Okay AI (2011) A regional olistostrome–mélange belt formed along a major strike–slip tear fault: Bornova Flysch Zone, western Turkey. Geophys Res Abstr 13:EGU2011-4689
Okay AI, Tüysüz O (1999) Tethyan sutures of northern Turkey. In: Durand B, Jolivet L, Horvath E, Seranne M (eds) The Mediterranean basins: tertiary extension within the Alpine orogen, vol 156. Geological Society, Special Publication, London, pp 475–515
Oyman T, Minareci F, Piskin O (2003) Efemcukuru B-rich epithermal gold deposit (Izmir, Turkey). Ore Geol Rev 23(1–2):35–53
Özeren MS, Holt WE (2010) The dynamics of the eastern Mediterranean and eastern Turkey. Geophys J Int 183(3):1165–1184. doi:10.1111/j.1365-246X.2010.04819.x
Özkaymak C, Sozbilir H (2008) Stratigraphic and structural evidence for fault reactivation: the active Manisa fault zone, western Anatolia. Turk J Earth Sci 17(3):615–635
Peddie NW (1982) International geomagnetic reference field: the third generation. J Geomagn Geoelectr 34(6):309–326
Pourteau A, Candan O, Oberhänsli R (2010) High-pressure metasediments in central Turkey: constraints on the Neotethyan closure history. Tectonics 29:TC5004. doi:10.1029/2009tc002650
Prelević D, Akal C, Foley S, Romer R, Stracke A, Van Den Bogaard P (2012) Ultrapotassic mafic rocks as geochemical proxies for post-collisional dynamics of orogenic lithospheric mantle: the case of southwestern Anatolia, Turkey. J Petrol 53(5):1019–1055
Purvis M, Robertson A (2005) Miocene sedimentary evolution of the NE–SW-trending Selendi and Gordes basins, W Turkey: implications for extensional processes. Sed Geol 174(1–2):31–62
Regnier JL, Ring U, Passchier CW, Gessner K, Gungor T (2003) Contrasting metamorphic evolution of metasedimentary rocks from the Cine and Selimiye nappes in the Anatolide belt, western Turkey. J Metamorph Geol 21(7):699–721
Ring U, Collins AS (2005) U–Pb SIMS dating of synkinematic granites: timing of core-complex formation in the northern Anatolide belt of western Turkey. J Geol Soc 162:289–298
Ring U, Gessner K, Gungor T, Passchier CW (1999) The Menderes Massif of western Turkey and the Cycladic Massif in the Aegean—do they really correlate? J Geol Soc 156:3–6
Ring U, Buchwaldt R, Gessner K (2004) Pb/Pb dating of garnet from the Anatolide Belt in western Turkey; regional implications and speculations on the role Anatolia played during the amalgamation of Gondwana. Zeitschrift der Deutschen Geologischen Gesellschaft 154(4):537–555
Salaün G, Pedersen HA, Paul A, Farra V, Karabulut H, Hatzfeld D, Papazachos C, Childs DM, Pequegnat C, Team S (2012) High-resolution surface wave tomography beneath the Aegean-Anatolia region: constraints on upper-mantle structure. Geophys J Int 190(1):406–420
Saunders P, Priestley KF, Taymaz T (1998) Variations in the crustal structure beneath western Turkey. Geophys J Int 134(2):373–389
Schermer ER, Lux DR, Burchfiel BC (1990) Temperature-time history of subducted continental crust, Mount Olympos Region, Greece. Tectonics 9(5):1165–1196
Sener AK, Arar M, Wedin F (2009) Contrasting styles of epithermal gold mineralisation at the Kiziltepe and Tavsan deposits, Western Turkey. In: Williams PJ et al. (ed) Smart science for exploration and mining, proceedings of the 10th Biennial meeting of The Society for Geology Applied to Mineral Deposits, Townsville, Australia, 17th–20th August 2009, vol 2, pp 848–850
Seyitoglu G, Scott BC (1996) The cause of N–S extensional tectonics in western Turkey: tectonic escape vs back-arc spreading vs orogenic collapse. J Geodyn 22(1–2):145–153
Sodoudi F, Kind R, Hatzfeld D, Priestley KF, Hanka W, Wylegalla K, Stavrakakis G, Vafidis A, Harjes H-P, Bohnhoff M (2006) Lithospheric structure of the Aegean obtained from P and S receiver functions. J Geophys Res 111:B12307
Sözbilir H, Inci U, Erkül F, Sümer Ö (2003) An active intermittent transform zone accommodating N–S extension in western Anatolia and its relation to the North Anatolian Fault System. In: International workshop on the North Anatolian, East Anatolian and Dead Sea Fault Systems Abstracts, vol., p 87
Thomson SN, Ring U (2006) Thermochronologic evaluation of post-collision extension in the Anatolide orogen, western Turkey. Tectonics 25(3):TC3005. doi:10.1029/2005tc001833
Tirel C, Gueydan F, Tiberi C, Brun J-P (2004) Aegean crustal thickness inferred from gravity inversion. Geodynamical implications for enrichment processes in the lithospheric mantle. J Volcanol Geotherm Res 96:127–147
Toker CE (2014) Geophysical analysis and modelling of the Simav basin, Western Anatolia. Bull Miner Res Explor 148:119–135
Ulugergerli E, Seyitoğlu G, Başokur A, Kaya C, Dikmen U, Candansayar M (2007) The geoelectrical structure of northwestern Anatolia, Turkey. Pure appl Geophys 164(5):999–1026
Uzel B, Sozbilir H (2008) A first record of a strike–slip basin in western Anatolia and its tectonic implication: the Cumaovasi basin. Turk J Earth Sci 17(3):559–591
Yigit O (2006) Gold in Turkey—a missing link in Tethyan metallogeny. Ore Geol Rev 28:147–179
Yigit O (2009) Mineral deposits of Turkey in relation to Tethyan metallogeny: implications for future mineral exploration. Econ Geol 104:19–51
Yilmaz H (1981) Genesis of uranium deposits in Neogene sedimetary rocks overlying the Menderes metamorphic massif, Turkey. Chem Geol 31:185–210
Yilmaz H, Oyman T, Arehart GB, Colakoglu AR, Billor Z (2007) Low-sulfidation type Au–Ag mineralization at Bergama, Izmir, Turkey. Ore Geol Rev 32:81–124
Zhu L, Akyol N, Mitchell BJ, Sozbilir H (2006) Seismotectonics of western Turkey from high resolution earthquake relocations and moment tensor determinations. Geophys Res Lett 33(7):L07316. doi:10.1029/2006gl025842
Zlatkin O, Avigad D, Gerdes A (2013) Evolution and provenance of Neoproterozoic basement and Lower Paleozoic siliciclastic cover of the Menderes Massif (western Taurides): coupled U–Pb–Hf zircon isotope geochemistry. Gondwana Res 23(2):682–700